

Article

# Effect of the Aerosol Type Selection for the Retrieval of Shortwave Ground Net Radiation: Case Study Using Landsat 8 Data

Cristiana Bassani <sup>1,\*</sup>, Ciro Manzo <sup>1</sup>, Ashraf Zakey <sup>2</sup> and Emilio Cuevas-Agulló <sup>3</sup>

<sup>1</sup> Institute of Atmospheric Pollution Research (IIA)-National Research Council (CNR), Research Area of Rome 1, Via Salaria Km 29,300, Monterotondo Scalo 00016, Rome, Italy; ciro.manzo@iia.cnr.it

<sup>2</sup> Egyptian Meteorological Authority (EMA), Koubry El-Quobba, Cairo 11784, Egypt; ashzakey@gmail.com

<sup>3</sup> Izaña Atmospheric Research Centre (AEMET), SC de Tenerife 38071, Spain; ecuevasa@aemet.es

\* Correspondence: cristiana.bassani@iia.cnr.it; Tel.: +39-06-9067-2398

Academic Editors: Giovanni Pitari and Robert W. Talbot

Received: 14 July 2016; Accepted: 14 August 2016; Published: 25 August 2016

**Abstract:** This paper discusses the aerosol radiative effects involved in the accuracy of shortwave net radiation,  $R_{n.sw}$ , with  $sw \in (400-900)$  nm, retrieved by the Operational Land Imager (OLI), the new generation sensor of the Landsat mission. Net radiation is a key parameter for the energy exchange between the land and atmosphere; thus,  $R_{n.sw}$  retrieval from space is under investigation by exploiting the increased spatial resolution of the visible and near-infrared OLI data. We adopted the latest version of the Second Simulation of a Satellite Signal in the Solar Spectrum (6SV) atmospheric radiative transfer model implemented in the atmospheric correction algorithm (OLI Atmospherically-Corrected Reflectance Imagery (OLI@CRI)) developed specifically for OLI data. The values of  $R_{n.sw}$  were obtained by varying the microphysical properties of the aerosol during the OLI@CRI retrieval of both the OLI surface reflectance,  $\rho_{pxl}^{oli}$ , and the incoming solar irradiance at the surface. The analysis of the aerosol effects on the  $R_{n.sw}$  was carried out on a spectrally-homogeneous desert area located in the southwestern Nile Delta. The results reveal that the  $R_{n.sw}$  available for energy exchange between the land and atmosphere reduces the accuracy (NRMSE  $\simeq 14\%$ ) when the local aerosol microphysical properties are not considered during the processing of space data. Consequently, these findings suggest that the aerosol type should be considered for variables retrieved by satellite observations concerning the energy exchange in the natural ecosystems, such as Photosynthetically-Active Radiation (PAR). This will also improve the accuracy of land monitoring and of solar energy for power generation when space data are used.

**Keywords:** aerosol; shortwave ground net radiation; atmospheric correction; Landsat; earth observation

## 1. Introduction

Natural and anthropogenic aerosols directly affect the energy exchange in the Earth-atmosphere coupled system by scattering and absorbing the solar radiation and indirectly by changing the lifetime and the microphysical properties of the clouds [1–3]. There are still uncertainties regarding the radiative effects of the atmospheric aerosol, and many efforts are underway to overcome the resulting errors on the energy exchange in natural ecosystems [4]. Concerning the direct effect, aerosols determine the direct and diffuse components of the radiation available at the surface for land-atmosphere energy exchange. A key parameter for energy exchange studies is the net radiation,  $R_n$ , which is defined by the difference between the incoming and the outgoing irradiance, which in turn depend on surface

parameters. The  $R_n$  is the total of shortwave ( $R_{n.sw}$ ) and longwave ( $R_{n.lw}$ ) radiation. The  $R_{n.sw}$  depends on the capability of the surface to reflect solar radiation (surface albedo), while the  $R_{n.lw}$  depends on the temperature and emissivity of the surface [5].

Remote sensing provides the spatial distribution of surface net radiation for both land use management and climate modeling.

To date, remote sensing data have restricted net radiation analysis to low spatial resolutions, as reported in [6]. On a global scale, in the 1985, the Earth Radiation Budget Experiment (ERBE), instruments on the Earth Radiation Budget Satellite (ERBS) [7] and then the Geostationary Earth Radiation Budget (GERB) [8] were designed with low spatial resolution specifically for studies on broadband net planetary energy. Later, the Clouds and the Earth's Radiant Energy System (CERES) was designed to follow the highly successful ERBE by increasing the spatial resolution to 20 km. The CERES surface radiation budget is retrieved by using the cloud and aerosol properties derived from the Moderate Resolution Imaging Spectroradiometer (MODIS) instrument [9,10], which is on-board the Earth Observing System (EOS) platforms. The POLARization and Directionality of the Earth's Reflectance (POLDER) is another useful sensor for this kind of study at a low spatial resolution (about 6 km) [11].

The most recent generation of Earth Observation sensors with improvements in terms of spectral and spatial resolution provides a new opportunity for the analysis of energy exchange in the Earth-atmosphere coupled system. Thus, the temporal and spatial combination of the new generation of the European Space Agency (ESA) [12] and the National Aeronautics and Space Administration (NASA) [13] sensors introduces a unique Earth observation system for systematic coverage at a medium resolution with a high revisit frequency of up to five days. Masek et al. [14] reported that the latest Landsat mission of NASA meets the requirements defined by the Global Climate Observing System (GCOS) for studying and monitoring land and coastal ecosystems. Indeed, the Operational Land Imager (OLI) sensor on-board Landsat 8 with a spatial resolution of 30 m in the shortwave spectral domain (visible to middle-infrared) is able to detect modifications of ecosystems by anthropic or natural sources [13].

Consequently, concerning the monitoring of ecosystems or the study of the energy exchange at the surface in the shortwave domain, remote sensing applications require the accurate simulation of the radiative effects of the aerosol on the shortwave net radiation,  $R_{n.sw}$ , available at the ground level for energy exchange between the surface and atmosphere [15]. Mira et al. [5] highlight the role of the surface albedo for  $R_{n.sw}$  retrieval using remote sensing data. Thus, the Bidirectional Reflectance Distribution Function (BRDF) of the surface is required as primary input for characterizing the anisotropy of the surface albedo depending on the zenith and the azimuth angles along illumination and viewing directions. The BRDF can be determined from data acquired by multi-view sensors, such as POLDER, to reconstruct the reflectance function directly from the measurements [16] or by coupling a measurement with kernel-driven models in the case of a sensor with a single view acquisition, such as MODIS [10]. The operational BRDF and albedo nadir reflectance products from MODIS data can be downloaded at no cost from the EOS Data Gateway (<http://eos.nasa.gov/imswelcome/>) and are described in Schaaf et al. [10] and Wanner et al. [17]. In all cases,  $R_{n.sw}$  is strictly connected to the surface and the aerosol physical properties, as explained in Mielonen et al. [18]. Both the surface albedo and aerosol influence the energy exchange between the biosphere and the atmosphere [19].

In order to retrieve the shortwave net radiation from space, the sensor radiance firstly needs to be converted to directional surface reflectance by the atmospheric correction processing [20,21]. This processing is mandatory for the assessment of spectral indices retrieved by remote sensing, such as the Photosynthetically-Active Radiation (PAR) and the Leaf Area Index (LAI) driven by the energy exchange and aimed at ecosystem productivity [22,23]. The accurate directional surface reflectance from remote sensing data is successfully achieved by physically-based atmospheric correction algorithms developed using radiative transfer models, such as the open-source 6SV1.1 [24,25], the latest version of the Second Simulation of a Satellite Signal in the Solar Spectrum (6S [26]) and MODTRAN

(Moderate Resolution Atmospheric Transmittance and Radiance) [27]. These models provide an accurate simulation of the solar radiation through the Earth-atmosphere coupled system by solving the radiative transfer equation [26,28]. If a ground station of the the AERONET worldwide network [29] is within the remote sensing image, the atmospheric correction can exploit the inverse products of the station by representing the microphysical properties of the aerosol [30,31], which improve the accuracy of the simulated radiative effects due to the aerosol [15,32,33]. The surface reflectance can thus be completely and accurately derived.

The accuracy of the surface reflectance retrieved from space very much depends on the correct modeling of the atmospheric scattering and absorption due to the aerosol [21]. The principal aerosol parameter of the radiative transfer model is the optical thickness of the aerosol at 550 nm,  $\tau_{550}$ , with robust and well-known retrieval algorithms for all of the above-mentioned sensors [24,34–37]. Other crucial parameters to simulate the radiative effects of the aerosol are the microphysical properties of the aerosol: the size distribution,  $dV(r)/dln(r)$ , and the real,  $Re_\lambda$  and the imaginary,  $Ri_\lambda$ , parts of the refractive index, integrated along the atmospheric column [38,39]. Unlike  $\tau_{550}$ , there is still no robust algorithm for the retrieval of the microphysical properties of the aerosol from space. Levy et al. [40] presents the global aerosol optical properties applied to MODIS for aerosol retrieval. Specifically, for the reflectance retrieval of dark surfaces, new aerosol models had to be introduced to improve the accuracy of the surface reflectance retrieved by atmospheric correction processing, as reported in Ahmad et al. [41]. Furthermore, in the case of strongly-absorbing aerosols with high aerosol optical thickness over a dark surface, also the aerosol profile needs to be considered for the high accuracy of the atmospheric correction products [42] by using data available from the several infrastructures [43–47].

We investigated the influence of the aerosol types with the default exponential vertical aerosol profile of the 6SVmodel, on the shortwave net radiation from OLI data by considering the OLI image atmospherically corrected with aerosol dust-like component as the benchmark, after validation with the reflectance MODIS product,  $\rho^{modis}$ . The results highlight that an accurate study and monitoring of the ecosystem is provided by new generation Earth Observation data if aerosol properties are taken into account. Thus, the aerosol radiative effects in terms of light absorption and scattering [28] could also be considered to analyze the uncertainty of the satellite-derived surface albedo products [19]. Our case study shows how a refined aerosol characterization reduces the uncertainties of the surface albedo and the shortwave net radiation from the new generation of the satellite remote sensing data.

## 2. Site and Data

### 2.1. Study Area

The study area was a very high reflective desert located in the southwestern Nile Delta, 70 km from Cairo (Figure 1), where an AERONET station was in operation. This desert area has a rectangular shape of 7.85 km  $\times$  5.5 km, with the centroid in 30°40'6.6''E and 29°53'57''N with an average height of 137 m. The target is of particular interest due to the Calibration and Validation (CAL/VAL) of the remote sensing products, such as surface reflectance. The geographical position also ensure the maximum illumination of the site, which is useful for the analysis of energy exchange. The closeness of the study area to an urban environment could be advantageous for the specific analysis of the radiative effects of anthropic aerosol on energy exchange.

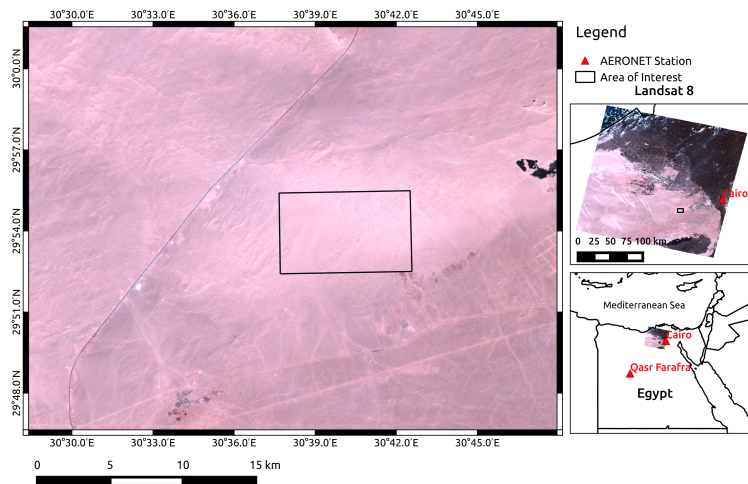


**Figure 1.** The rectangle is the study area located in the southwestern Nile Delta. The geographical coordinates in the reference system WGS84 are shown along the border of the map. The AERONET stations are shown by red triangles.

## 2.2. Data

### 2.2.1. OLI and MODIS Data

The remote sensing data employed were available on EarthExplorer, the long-term archive of USGS (<http://earthexplorer.usgs.gov/>). Two sun-synchronous sensors were considered (Table 1): the Moderate Resolution Imaging Spectroradiometer (MODIS) on board EOS AM-1 (Terra) and the Optical Land Imager (OLI) on board the Landsat 8 satellite. These sensors differ in terms of the revisit time (1 day for MODIS vs. 16 days for OLI) and the spatial resolution of 250 m (Bands 1–2), 500 m (Bands 3–7) for MODIS and 30 m for the OLI (Band 1–7), respectively.

**Table 1.** Spectral and spatial characteristics of MODIS and OLI sensors. The MODIS Bands 1 and 2 have a resolution of 250 m, while the MCD43A1 has a resolution of 500 m.

MODIS Band Number	MODIS Bandwidth	MODIS Spatial Res (m)	OLI-L8 Band Number	OLI-L8 Bandwidth	OLI-L8 Spatial Res (m)
3	459–479	500	B1—Coastal aerosol	430–450	30
4	545–565	500	B2—Blue	450–510	30
1	620–670	250 (500)	B3—Green	530–590	30
2	841–876	250 (500)	B4—Red	640–670	30
5	1230–1250	500	B5—Near infrared (NIR)	850–880	30
6	1628–1652	500	B6—Shortwave IR (SWIR 1)	1570–1650	30
7	2105–2155	500	B7—SWIR 2	2110–2290	30

6 December 2015 was selected to ensure the concurrent availability of OLI at 8:30 GMT and MODIS products derived from the image acquired at 9:35 GMT. The meteorological conditions when Landsat passed over the study area showed low cloud cover with a temperature of 13°, wind speed of 4.6 m/s and direction ENE. The OLI data were collected in Path 177 Row 039 at the level of processing L1T (terrain corrected) and were in the reference system WGS84 projection UTM 36. The MOD09GA and MCD43A1 products of the MODIS sensor were downloaded considering the tile h20 and v06. MOD09GA is the surface reflectance in a daily gridded L2G product with spatial resolution of 500 m and sinusoidal projection (LPDAAC). The MCD43A1 product contains the BRDF parameters to derive the albedo by a three-dimensional system composed of isotropic, volumetric and surface scattering components (iso, vol, geo) for each MODIS band. The BRDF parameters are derived over

a 16-day period describing the surface anisotropy of each pixel with a spatial resolution of 500 m and sinusoidal projection.

### 2.2.2. AERONET Data

The AERONET network [29] provides direct and inverse products (<http://aeronet.gsfc.nasa.gov/>) derived from the radiative measurements performed by the automatic Cimel Sun sky-radiometer [30]. These products are the integrated columnar values of atmospheric parameters, which are adopted to simulate the atmospheric radiative effects on the solar radiation propagating through the atmosphere by radiative transfer models, such as 6SV [25]. In this study, the direct and inverse products from the AERONET stations in Cairo and El Farafra 400 km from the test site were used as the closest atmospheric state measurements to the considered OLI image in space and time. The two AERONET stations are taken into consideration for aerosol characterization for the distance (El Cairo) and the environment (El Farafra). El Cairo is the closest station to the site and located in a urban environment, whereas El Farafra station is far from the study area, but in the same environment (i.e., desert).

Table 2 reports the direct products retrieved from the Sun-radiance measurements (at Level 1.5). The aerosol optical thickness at 550 nm,  $\tau_{550}$ , is the principal aerosol parameter investigated from space [24,34–36,48,49].  $\tau_{550}$  was derived by applying exponential interpolation between the two nearest aerosol optical thicknesses  $\tau_{440}$  at 440 nm and  $\tau_{870}$  at 870 nm available from the two AERONET stations at the OLI overpass time.

**Table 2.** Direct products of the AERONET stations in Cairo and El Farafra closest in time to the OLI image considered in this study (6 December 2015).

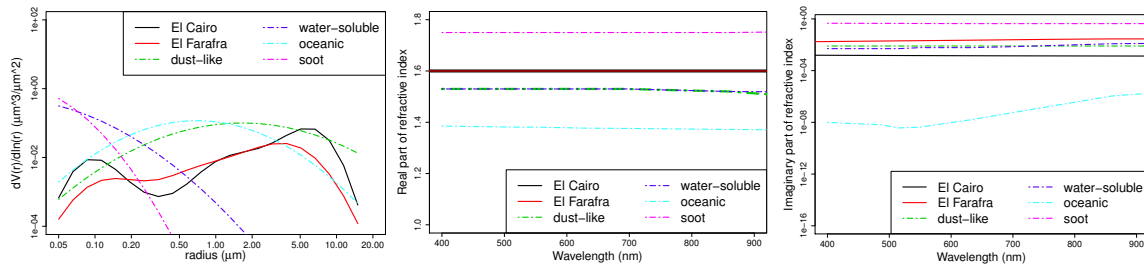
	Aerosol Optical Thickness at 550 nm $\tau_{550}$	Water Vapor $wv$ (cm)	Ozone $o3$ (Db)
Cairo (9:46 GMT)	0.074	0.743	0.276
El Farafra (7:44 GMT)	0.122	0.469	0.264

Table 2 shows low values of  $\tau_{550}$  in the two AERONET stations, revealing that aerosol events did not occur during the Landsat overpass.  $wv$  and  $o3$  represent the columnar content of water vapor and ozone, respectively. Both atmospheric parameters principally influence the radiative transfer within the absorption bands of the water vapor and ozone, which are outside the OLI channels considered in this study.

The plots in Figure 2 show the inverse products of the two AERONET stations [32] (at Level 1.5) and the microphysical properties of the basic components included in the 6SV model (dust-like, water-soluble, oceanic and soot) [25]. On the left, the plot shows the volumetric size distribution of the aerosol types considered in this study,  $dV(r)/d\ln(r)$ . As expected for a desert site, a coarse mode-dominated distribution was measured in El Farafra. The trimodal distribution in Cairo is combined by the nuclei and the accumulation modes (fine particles) and the coarse mode, the usual pattern of size distribution in urban sites, as explained on in Kokhanovsky et al. [49].

The centered plot in Figure 2 shows the real part of the refractive index,  $Re$ , for each aerosol type considered. The real parts for the dust-like and water-soluble components are similar as in the case of the inverse products of the Cairo and El Farafra stations ( $Re = 1.6$ ). The  $Re$  values of soot and oceanic are furthest away from the Cairo and El Farafra products and probably less representative of the local aerosol.

Concerning the imaginary parts of the refractive index,  $Ri$ , reported on the right in Figure 2, all of the aerosol types presented the  $Ri$  as being low sensitive to wavelength as in the case of the  $Re$ , with the exception of the  $Ri$  of the oceanic component. The oceanic component has low  $Ri$ , leading to negligible absorption of the solar radiation at the visible spectral domain.



**Figure 2.** The microphysical properties of the aerosol available from AERONET stations in Cairo and El Farafra measured close in time to the Landsat overpass (Table 2) and the microphysical properties of the aerosol basic components reported in [25]. On the left, the volumetric size distribution; in the center, the real part of the refractive index; on the right, the imaginary part of the refractive index.

### 3. Methodology

The radiative effects of the aerosol on the  $R_{n,sw}$  retrieved from space were investigated as outlined in Figure 3.

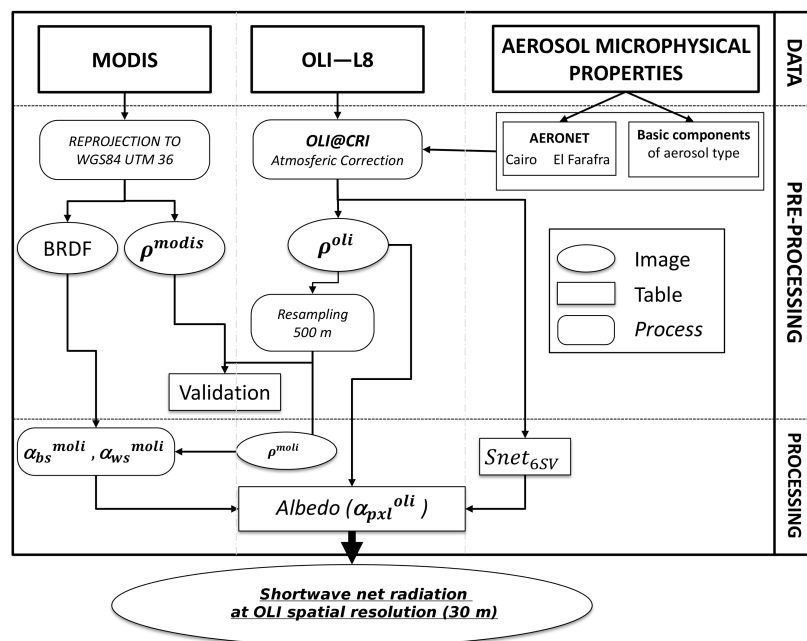


**Figure 3.** Processing chain for retrieval of the  $R_{n,sw}$  at OLI spatial resolution.

The core component is the surface albedo achieved pixel-by-pixel from the OLI image. The surface albedo,  $\alpha_{pxl}^{oli}$ , was assessed following Shuai et al. [50] combining Landsat surface reflectance,  $\rho^{oli}$ , with MODIS surface anisotropy products (BRDF) and black and white albedo ( $\alpha_{bs}^{moli}$ ,  $\alpha_{ws}^{moli}$ ) under the assumption of a spectral homogeneous desert area. The surface reflectance was retrieved by a physically-based algorithm developed for the atmospheric correction of OLI images, OLI Atmospherically-Corrected Reflectance Imagery (OLI@CRI) using the 6SV model. The algorithm was implemented to work with the microphysical properties of the aerosol available as AERONET inverse products or with the microphysical properties of four aerosol basic component included in the 6SV model (dust-like, water-soluble, oceanic, soot) [25] considering an exponential vertical distribution of the aerosol with a scale height of 2 (default aerosol profile of 6SV model).

Using this algorithm, the OLI image was atmospherically corrected with different aerosol types. The OLI corrected images were compared to the concurrent MODIS surface reflectance product in order to validate the OLI reflectance, as suggested in [51]. The albedo was achieved by combining OLI surface reflectance with MODIS surface anisotropy information [50]. Finally, the  $R_{n,sw}$  was obtained by the equation expressed in Mira et al. [5] for all of the aerosol types within the OLI channels in the spectral domain 400–900 nm.

### 3.1. OLI@CRI Atmospheric Correction Algorithm

The OLI@CRI algorithm was developed for the atmospheric correction processing of the OLI images specifically over land following the procedure described in [38,48] adapting the vector version of the Second Simulation of a Satellite Signal in the Solar Spectrum (6SV) radiative transfer model. This model is the improved version of the 6S used for the new generation of atmospheric correction algorithms, which was successfully adopted by [52]. The algorithm was implemented with the open-source GNU data language (GDL) [53] and works with the OLI image available in L1T format. As with the previous algorithms [38,39,48], OLI@CRI can be applied by considering the standard aerosol basic components (dust-like, water-soluble, oceanic and soot [25]) provided by default by the 6SV model or the microphysical properties of the aerosol provided by an AERONET station as inverse products. The OLI@CRI algorithm overcomes the limits of software such as Landsat Ecosystem Disturbance Adaptive Processing System (LEDAPS) [14], where a continental aerosol model is assumed for atmospheric correction processing and an over-correction of the surface reflectance is expected. LEDAPS therefore restricts the potential of the remote sensing data by excluding the microphysical properties of the aerosol. Indeed, the aerosol optical properties required for accurate radiative modeling during the atmospheric correction are derived from the observed microphysical properties by the Mie theory solved in the 6SV model [25] (p. 108).

As usual, the ground reflectance at the  $\lambda$  wavelength with solar illumination ( $\theta_s, \phi_s$ ) and sensor viewing ( $\theta_v, \phi_v$ ) directions is expressed by [21,24,26]:

$$\rho_{gnd}(\lambda, \theta_s, \phi_s, \theta_v, \phi_v) = \frac{t_g \rho_{atm} - \rho_{TOA}}{S(t_g \rho_{atm} - \rho_{TOA}) - t_s t_g} \quad (1)$$

where  $\rho_{TOA} = \pi L_v / \mu_s E_s$  is the sensor reflectance expressed by the TOA (Top Of Atmosphere) solar irradiance,  $E_s$ . The  $\mu_{v,s} = \cos(\theta_{v,s})$  are the cosine of the view ( $v$ ) and Sun ( $s$ ) zenith angles to define the illumination and viewing directions. The  $\theta_{v,s}$  is the view ( $v$ ) and Sun ( $s$ ) azimuth angles.  $t_g$  is the gas transmittance;  $\rho_{atm}$  is the atmospheric reflectance;  $S$  is the atmospheric spherical albedo [28];  $t_s = t^\uparrow + t^\downarrow$  represents the total transmittance obtained from the downward and upward directions; and finally,  $t^{\uparrow,\downarrow} = e^{-\tau(\lambda)/\mu_{v,s}} + t_{dif}^{\uparrow,\downarrow}$  is the transmittance of up and down directions composed of direct and diffuse component depending on the total optical thickness due to the aerosol and molecules ( $\tau$ ). The 6SV model [24] is implemented in OLI@CRI to simulate all of the radiative quantities of Equation (1) in the 400–900-nm spectral domain with a sampling of 2.5 nm. The OLI@CRI algorithm computes the convolution of the radiative quantities on the spectral response of the OLI sensor reported in Barsi et al. [54], following the procedure described in [48].

The surface reflectance,  $\rho_{pxl}^{oli}(\lambda, \theta_s, \phi_s, \theta_v, \phi_v)$ , is retrieved by removing the effect of the neighboring pixels into the pixel viewed from the sensor (adjacency effect) by the empirical formula [21,24,26]:

$$\rho_{pxl}^{oli}(\lambda, \theta_s, \phi_s, \theta_v, \phi_v) = \rho_{gnd} + \frac{t_{dif}^\uparrow}{e^{-\tau(\lambda)/\mu_v}} [\rho_{gnd} - \langle \rho_{gnd} \rangle] \quad (2)$$

where the  $\langle \rho_{gnd} \rangle$  is the mean of the pixel adjacent to the viewing pixel covering the entire swath of the OLI sensor.

### 3.2. Albedo

The albedo,  $\alpha_{oli}(\lambda, \theta_s)$ , was obtained following Shuai et al. [50], where the surface anisotropy is solved at OLI spatial resolution starting from the MODIS spatial resolution. The albedo was considered in the OLI channels in the visible spectral domain, which is more sensitive to the radiative impact of the aerosol. The homogeneous area was chosen at MODIS and OLI spatial resolutions to meet the hypothesis in Shuai et al. [50]. The generation of the Landsat albedo [50] is based on the kernel-driven reciprocal RossThick-LiSparseBRDF model used in the MODIS algorithm for albedo retrieval [10,17,25].

$$\rho_\lambda(\theta_v, \theta_s, \phi) = f_{iso,\lambda} + f_{vol,\lambda}K_{vol,\lambda}(\theta_v, \theta_s, \phi) + f_{geo,\lambda}K_{geo,\lambda}(\theta_v, \theta_s, \phi) \quad (3)$$

where  $K_{vol,\lambda}(\theta_v, \theta_s, \phi)$  is the volume-scattering Ross-Thick kernel and  $K_{geo,\lambda}(\theta_v, \theta_s, \phi)$  is the surface-scattering LiSparse kernel.  $f_{iso,\lambda}$ ;  $f_{vol,\lambda}$  and  $f_{geo,\lambda}$  are the parameters of the three-dimensional MCD43A1 product available for each MODIS band. These parameters were reprojected in the same reference system (WGS84 projection UTM fuse 36) of the OLI image. Based on Equation (3), both the albedo due to the direct solar beam without diffuse component, black-sky albedo  $\alpha_{bs}^{modis}(\theta, \lambda)$  and the albedo due to the diffuse component of the solar beam without the direct component, white-sky albedo  $\alpha_{ws}^{modis}(\lambda)$ , are generated by the following expression [10]:

$$\begin{aligned} \alpha_{bs,ws}^{modis}(\theta_s, \lambda) = & f_{iso,\lambda}(g_{0iso}^{b,w} + g_{1iso}^{b,w}\theta_s^2 + g_{2iso}^{b,w}\theta_s^3) + \\ & f_{vol,\lambda}(g_{0vol}^{b,w} + g_{1vol}^{b,w}\theta_s^2 + g_{2vol}^{b,w}\theta_s^3) + \\ & f_{geo,\lambda}(g_{0geo}^{b,w} + g_{1geo}^{b,w}\theta_s^2 + g_{2geo}^{b,w}\theta_s^3) \end{aligned} \quad (4)$$

where  $f_{iso,\lambda}$ ;  $f_{vol,\lambda}$  and  $f_{geo,\lambda}$  are explained in Equation (3) and  $\theta_s$  is the solar zenith angle at Landsat acquisition time as explained in [50]. The  $g_{ik}$  terms in Equation (4) are reported in Table 3.

**Table 3.** Coefficients of Equation (4) reported in Schaaf et al. [10].

$g_{jk}$ for Kernel $k$	Isotropic ( $k = iso$ )		RossThick ( $k = vol$ )		LiSparse-R ( $k = geo$ )	
	Black-Sky	White-Sky	Black-Sky	White-Sky	Black-Sky	White-Sky
$g_{0k}$	1.0	1.0	-0.007574	0.189184	-1.284909	-1.377622
$g_{1k}$	0.0	0.0	-0.070987	0.0	-0.166314	0.0
$g_{2k}$	0.0	0.0	0.307588	0.0	0.041840	0.0

Shuai et al. [50] introduced the ratio between the albedo and reflectance, with the geometrical acquisition of Landsat, resampled to MODIS spatial resolution for albedo retrieval at Landsat resolution:

$$a_{bs}^{moli}(\lambda, \theta_s, \theta_v, \phi) = \alpha_{bs}^{modis}(\theta_s, \lambda) / \rho^{moli}(\lambda, \theta_s, \theta_v, \phi) \quad (5)$$

$$a_{ws}^{moli}(\lambda, \theta_s, \theta_v, \phi) = \alpha_{ws}^{modis}(\lambda) / \rho^{moli}(\lambda, \theta_s, \theta_v, \phi) \quad (6)$$

where  $\rho^{moli}(\lambda, \theta_s, \theta_v, \phi)$  is the OLI surface reflectance obtained from Equation (2) resampled to MODIS spatial resolution. Under the hypothesis of a homogeneous area, verified by the desert area chosen for this study, Shuai, Y. et al. [50] affirmed that the ratio at MODIS spatial resolution is similar to the ratio at Landsat spatial resolution,  $a_{bs}^{moli}(\lambda, \theta_s, \theta_v, \phi) \sim a_{bs}(\lambda, \theta_s, \theta_v, \phi)$  and  $a_{ws}^{moli}(\lambda, \theta_s, \theta_v, \phi) \sim a_{ws}(\lambda, \theta_s, \theta_v, \phi)$ . Thus, white-sky and black-sky albedo at Landsat resolution are:

$$\alpha_{bs}(\theta_s, \lambda) = a_{bs}^{moli}(\lambda, \theta_s, \theta_v, \phi) \rho^{oli}(\lambda, \theta_s, \theta_v, \phi) \quad (7)$$

$$\alpha_{ws}(\lambda) = a_{ws}^{moli}(\lambda, \theta_s, \theta_v, \phi) \rho^{oli}(\lambda, \theta_s, \theta_v, \phi) \quad (8)$$

Finally, the albedo at Landsat spatial resolution for each pixel,  $\alpha_{pxl}^{oli}(\theta_s, \lambda)$ , is retrieved following [15]:

$$\alpha_{pxl}^{oli}(\theta_s, \lambda) = [1 - Snet_{6SV}(\theta_s, \tau_{550}, aer.phys_{\lambda})]\alpha_{bs}(\theta_s, \lambda) + Snet_{6SV}(\theta_s, \tau_{550}, aer.phys_{\lambda})\alpha_{ws}(\lambda) \quad (9)$$

where  $\alpha_{bs}(\theta, \lambda)$  is the black-sky albedo and  $\alpha_{ws}(\lambda)$  is the white-sky albedo. The  $Snet_{6SV}(\theta_s, \tau_{550}, aer.phys_{\lambda})$  is the ratio of the diffuse albedo on the total component of solar radiation simulated by the 6SV model at Landsat acquisition time (solar zenith angle  $\theta_s$ ), with the aerosol optical thickness at 550 nm of the Cairo AERONET station and considering the microphysical properties of the aerosol,  $aer.phys_{\lambda}$ , as downloaded from AERONET stations in Cairo and El Farafra and referring to the aerosol basic components (dust-like, water-soluble, oceanic and soot [25]).

### 3.3. Shortwave Net Radiation, $R_{n.sw}$

The instantaneous shortwave net radiation at ground level in the spectral domain 400–900 nm,  $R_{n.sw}$ , is achieved by the equation introduced in Mira et al. [5] limited to the visible and near-infrared components where the radiative effects of the aerosol are stronger than any of those in other spectral domains:

$$R_{n.sw,\lambda} = (1 - \alpha_{oli}(\theta_s, \lambda))R_{sw,\lambda}^{\downarrow} \quad (10)$$

where  $R_{sw}^{\downarrow}$  is the at ground total component of the downward solar irradiance, including direct and diffuse components;  $\alpha_{oli}(\theta_s, \lambda)$  is the surface albedo at  $\lambda$  wavelength and illuminated at  $\theta_s$  angle. The  $R_{sw}^{\downarrow}$  can be measured by using specific instruments or simulated by using an atmospheric radiative transfer model, such as 6SV. As reported in Shuai et al. [50], the aerosol is a source of errors for  $R_{sw}^{\downarrow}$  assessment. The  $\alpha_{oli}(\theta_s, \lambda)$  can be very accurately and reliably derived from the surface reflectance if the microphysical properties of the aerosol are taken into account during the atmospheric correction of the remote sensing data [39,55].

## 4. Results

### 4.1. OLI Surface Reflectance, $\rho_{pxl}^{oli}$

The OLI@CRI algorithm was applied to the OLI image acquired over the desert area under six atmospheric conditions defined by the AERONET inverse products available from the Cairo and El Farafra stations and by the size distribution and refractive index of the four aerosol basic components included in 6SV (dust-like, water-soluble, oceanic and soot [25]).

The  $\tau_{550}$ , the water vapor and the ozone columnar contents were fixed to the direct products of the AERONET station in Cairo since this was the closest to the study area. These atmospheric parameters were changed to the direct products of the AERONET station only when the OLI@CRI algorithm was applied to the OLI image with El Farafra atmospheric conditions.

#### 4.1.1. Validation with MODIS Reflectance Product

The six atmospherically-corrected OLI images were resampled at MODIS spatial resolution to validate the OLI surface reflectance with the MODIS surface reflectance product (MOD09GA). The OLI resampling was performed in the selected area (Desert B type in Figure 4), which verified the spectral homogeneity conditions for the generation of Landsat albedo [50] and the condition of lower cloud cover with maximum insolation to evaluate the radiative impact of the aerosol on  $R_{n.sw}$ . The homogeneous area was selected by the K-means unsupervised classification, which identified a spectral cluster of pixels depending on the land cover classes. The Desert B type (Figure 4) was selected as the highest reflective class in the image.

Figure 5 shows the six resampled OLI surface reflectances,  $\rho^{moli}(\lambda, \theta_s, \theta_v, \phi)$ , and the MODIS reflectance products of the study area. The MODIS reflectance was considered as the benchmark to

identify the most suitable aerosol type to validate the OLI reflectance. The nearest OLI reflectance to the MODIS product is obtained in the case of dust-like microphysical properties, while the case of Cairo inverse products is the most distant from the MODIS reflectance. This effect is similar to the aerosol condition described in Bas et al. [39], where the role of a tri-modal size distribution on the accuracy of retrieved surface reflectance from space needs to be investigated.

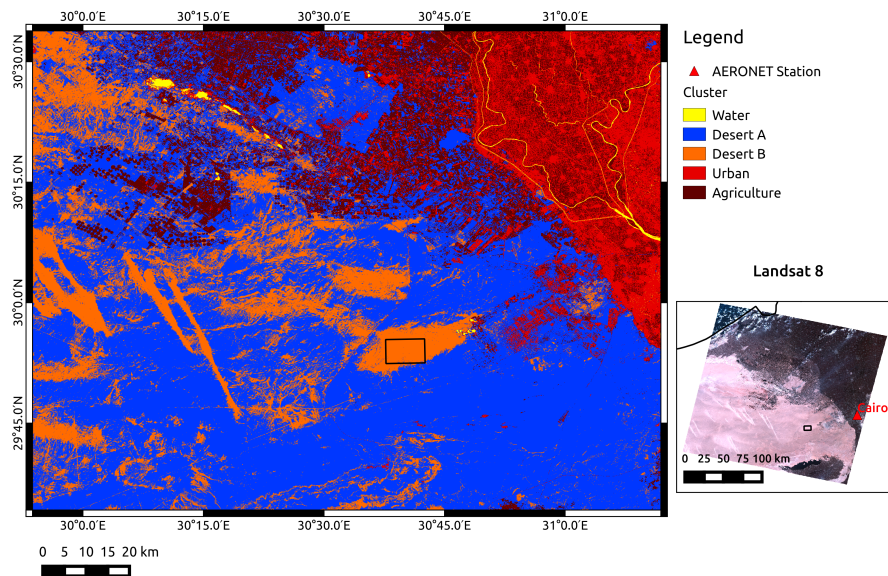


Figure 4. Unsupervised classification of the study area with main land cover clusters.

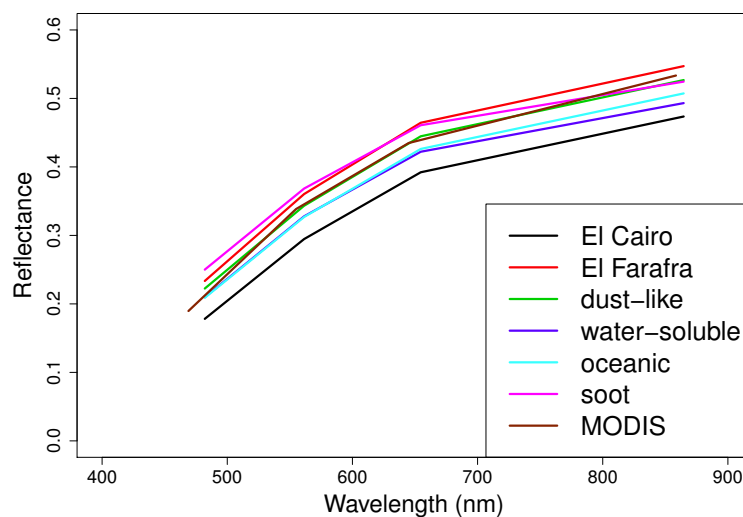


Figure 5. The OLI surface reflectance retrieved by applying of the OLI Atmospherically-Corrected Reflectance Imagery (OLI@CRI) algorithm considering the aerosol microphysical properties as the inverse products of Cairo and El Farafra AERONET stations and as the four basic component included in the 6SVmodel (dust-like, water-soluble, oceanic and soot [25]).

Table 4 shows the Normalized Root Mean Square Error (NRMSE) of the OLI surface reflectance of Figure 5 considering the MODIS surface reflectance of the study area as the benchmark. The NRMSE confirmed that the OLI surface reflectance nearest to the MODIS one is obtained with the dust-like

aerosol. In fact, the NRMSE for dust-like aerosol (NRMSE-dl) is lower than the others. The NRMSE for oceanic (NRMSE-oc) close to the NRMSE-dl confirms the crucial role of the size distribution of the radiative impact over a bright surface. The NRMSE for water-soluble (NRMSE-ws) is less than for soot (NRMSE-so).

**Table 4.** Normalized Root Mean Square Error (NRMSE) of the six OLI surface reflectance obtained by OLI@CRI with the available microphysical properties of the aerosol: Cairo, El Farafra and the four basic components (dl for dust-like; ws for water-soluble; oc for oceanic; so for soot) with respect to the MOD09GA MODIS product on the study area.

NRMSE-Cairo %	NRMSE-El Farafra %	NRMSE-dl %	NRMSE-ws %	NRMSE-oc %	NRMSE-so %
11.5	7.9	4.7	6.4	4.8	9.7

#### 4.2. OLI Albedo

The surface albedo,  $\alpha_{pxl}^{oli}(\theta_s, \lambda)$ , was retrieved using the  $\rho^{oli}(\lambda, \theta_s, \theta_v, \phi)$  and the MODIS products, which are the BRDF parameters, for each one of the six atmospherically-corrected OLI images.

Table 5 reports the surface albedo averaged by the pixels over the study area, for the OLI channels overlapping the MODIS ones. Table 5 showed that the second, third and fourth channels (from the first to third column) in the El Cairo station, water-soluble and oceanic are equal to the lowest values, while soot has the highest values. El Farafra has similar values to soot in the forth channel. The fifth band has the highest variability of values; in this channel, El Farafra has the highest albedo. These results highlight that dust-like is different in the spectral range 482–654 nm, while at 864 nm, it has values comparable to soot. Moreover, the results obtained by AERONET microphysical properties supply different results, confirming that the different microphysical conditions at a long distance provide a difference in albedo values. The microphysical properties of the soot clearly led to a different capability of the surface to reflect the solar radiation with regard to the capability obtained with the other aerosol types.

**Table 5.** Surface albedo averaged by the pixels over the study area at Landsat resolution for the second to the fifth OLI channels. The values refer to the surface albedo obtained from the OLI image atmospherically corrected with AERONET inverse products and the microphysical properties of the four basic components of the aerosol included in 6SV (dust-like, water-soluble, oceanic, soot [25]).

Aerosol Types	$\alpha_{II}$ (482.04 nm)	$\alpha_{III}$ (561.41 nm)	$\alpha_{IV}$ (654.59 nm)	$\alpha_V$ (864.67 nm)
Cairo station	0.18	0.49	0.40	0.49
El Farafra station	0.20	0.54	0.44	0.54
Dust-like	0.19	0.51	0.42	0.52
Water-soluble	0.18	0.49	0.40	0.49
Oceanic	0.18	0.49	0.40	0.50
Soot	0.21	0.55	0.44	0.52

#### 4.3. Shortwave Net Radiation at 30-m Spatial Resolution

$R_{n.sw}$  was solved pixel-by-pixel by Equation (10) after the retrieval of the  $Snet_{6SV}(\theta_s, \tau_{550}, aer.phys_\lambda)$ . Table 6 reports the  $Snet_{6SV}(\theta_s, \tau_{550}, aer.phys_\lambda)$  over the study area for the second to the fifth OLI channels, simulated by the 6SV model for the aerosol microphysical properties as the inverse products of the Cairo and El Farafra AERONET stations and as the basic components of the aerosol included in 6SV (dust-like, water-soluble, oceanic, soot [25]). The lowest  $Snet_{6SV}(\theta_s, \tau_{550}, aer.phys_\lambda)$  is for the microphysical properties of the soot, whereas the highest values are for the El Farafra inverse products.

Table 7 shows  $R_{n.sw}$  averaged by the pixels over the study area at Landsat resolution for the OLI channel overlapping the MODIS channels (as in Table 6).  $R_{n.sw}$  was achieved for the six images

resulting from the atmospheric correction of the OLI image using the six aerosol types defined by the microphysical properties considered in this study: the AERONET inverse products available from the Cairo and El Farafra stations and the four basic components of the aerosol included in 6SV (dust-like, water-soluble, oceanic, soot [25]).

**Table 6.**  $Snet_{6SV}(\theta_s, \tau_{550}, aer.phys_\lambda)$  over the study area for the second to the fifth OLI channel, simulated by the 6SV model for the aerosol microphysical properties as the inverse products of the Cairo and El Farafra AERONET stations and as the basic components of the aerosol included in 6SV (dust-like, water-soluble, oceanic, soot [25]).

Aerosol Types	$Snet_{II}$ (482.04 nm)	$Snet_{III}$ (561.41 nm)	$Snet_{IV}$ (654.59 nm)	$Snet_V$ (864.67 nm)
Cairo station	0.24	0.17	0.12	0.08
El Farafra station	0.26	0.20	0.15	0.12
Dust-like	0.21	0.16	0.12	0.10
Water-soluble	0.24	0.17	0.12	0.06
Oceanic	0.24	0.18	0.15	0.13
Soot	0.16	0.09	0.05	0.02

**Table 7.**  $R_{n.sw}$  averaged by pixels at Landsat spatial resolution over the study area. The  $R_{n.sw}$  is reported for the OLI channels (the second to the fifth) overlapping the MODIS channels.

Aerosol Types	$R_{n.swII}$ (W/m <sup>2</sup> /μm) (482.04 nm)	$R_{n.swIII}$ (W/m <sup>2</sup> /μm) (561.41 nm)	$R_{n.swIV}$ (W/m <sup>2</sup> /μm) (654.59 nm)	$R_{n.swV}$ (W/m <sup>2</sup> /μm) (864.67 nm)
Cairo station	786.1	468.8	497.2	281.2
El Farafra station	730.9	404.3	442.9	239.8
Dust-like	763.2	438.2	468.9	256.4
Water-soluble	789.7	470.1	498.0	281.5
Oceanic	803.4	476.6	498.9	274.6
Soot	671.9	376.0	433.3	250.4

The accuracy of the OLI shortwave net radiation,  $R_{n.sw}$ , and surface reflectance,  $\rho_{pxl}^{oli}$ , products was evaluated by the NRMSE of the products obtained for each aerosol type condition with respect to the dust-like basic component values validated with the MODIS reflectance product. The  $\rho^{oli}$  was retrieved from the  $\rho_{pxl}^{oli}$  averaged by the pixels over the study area. Table 8 reports both NRMSEs achieved using all of the OLI channels (the second to the fifth) overlapping the MODIS channels.

**Table 8.** NRMSE of the shortwave net radiation,  $R_{n.sw}$ , and the surface reflectance,  $\rho^{oli}$ , obtained for each aerosol condition with respect to the values in the dust-like reference case over the study area. The NRMSEs were achieved considering the second to the fifth OLI channels.

NRMSE. Product	Cairo Station %	El Farafra Station %	Water-Soluble %	Oceanic %	Soot %
NRMSE. $\rho^{oli}$	16.8	5.6	7.9	5.7	7.4
NRMSE. $R_{n.sw}$	5.3	5.7	5.6	6.2	13.8

### 5. Discussion and Conclusions

This paper discusses the aerosol impacts on the net radiation in the shortwave,  $R_{n.sw}$ , from space applying the procedure for  $R_{sw.n}$  retrieval by Equation (10) [5] over the study area, which satisfied the condition of maximum illumination and minimum cloud cover on a bright surface, as well as the requirement of spectral homogeneity (Figure 4) for Landsat albedo generation [50]. The procedure for the albedo retrieval [50] (Section 3.2) is based on Equation (9) and involved concurrently MODIS products (BRDF,  $\alpha_{ws}$  and  $\alpha_{bs}$  in Section 3.2) and OLI surface reflectance ( $\rho_{pxl}^{oli}$  in Section 3.1). The OLI surface reflectance was retrieved by applying the OLI@CRI algorithm described

in Section 4.1. The atmospheric correction of the OLI image was performed using the inverse products of the two AERONET stations and the microphysical properties of the four aerosol basic components included in 6SV (dust-like, water-soluble, oceanic and soot) [25]. The NRMSE of the six OLI surface reflectances obtained with the six aerosol conditions was achieved with respect to the MODIS image for the overlapping MODIS and OLI channels as reported in Table 4. The surface reflectance retrieved by considering the microphysical properties of the dust-like case produced lower NRMSE with respect to the MODIS surface reflectance (Table 4). Consequently, the influence of the aerosol conditions on the accuracy of  $\rho_{pxl}^{oli}$  in the study area was performed considering  $\rho_{pxl}^{oli}$  in the dust-like case as the validated surface reflectance.

The results highlight that the radiative impact of the aerosol plays a crucial role in the accuracy of the surface reflectance,  $\rho_{pxl}^{oli}$ , and the shortwave net radiation,  $R_{n.sw}$ , achieved through OLI data. The use of these remote sensing products needs to take into account the aerosol type considered during the data processing. Indeed, the microphysical properties are the main issue for aerosol characterizations with respect to their radiative impact on remote sensing data, specifically in the atmospheric window. Table 2 shows low values of  $\tau_{550}$  in the two AERONET stations, revealing that aerosol events did not occur during the Landsat overpass. Hence, a low variability in the radiative impact due to different aerosol types is expected, whereas a great influence of  $wv$  and  $o3$  is not expected, because their respective absorption bands are outside the OLI channels considered in this study.

The NRMSE of the OLI surface reflectance over the study area (NRSME. $\rho^{oli}$  in Table 8 in Section 4.3) shows that the accuracy of the bright surface reflectance depends principally on the volumetric size distribution,  $dV(r)/dln(r)$ . The lower NRSME. $\rho^{oli}$  in Table 8 is in the case of the coarse components, oceanic and El Farafra aerosol in Figure 2. Oceanic is the aerosol basic component composed of the coarse mode as the dust-like and the bi-modal size distribution of the aerosol measured in El Farafra consist mainly of the coarse mode. The other NRSME. $\rho^{oli}$  in Table 8 increases in the case of fine aerosol, water-soluble and soot components. The maximum NRSME. $\rho^{oli}$  is achieved when a tri-modal size distribution characterizes the aerosol Cairo in Figure 2). As expected, the NRMSE of the OLI reflectance obtained with the AERONET products cannot be similar, since the stations are located in different environments (urban and desert) with their respective microphysical properties of the aerosol (cf. Figure 2) Concerning the absorption of solar radiation, the imaginary part of the refractive index led to a separation between the solar radiation absorption by the aerosol type with low NRSME. $\rho^{oli}$  (oceanic component and El Farafra). The oceanic component is non-absorbing aerosol, as confirmed by the very low imaginary part of the refractive index (right plot in Figure 2). On the other hand, the dust-like component and El Farafra aerosol are absorbing aerosol with a spectrally flat imaginary part of the refractive index in the visible spectral domain ( $R_i = 0.008$  in Vermote et al. [25,28]). Thus, the refractive index seems to be the most negligible aerosol property for  $\rho^{oli}$  retrieval in the case of a bright surface.

Nevertheless, the absorption of solar radiation plays a significant role in the retrieval of remotely-sensed products connected with land-atmosphere energy exchange, such as shortwave net radiation. The higher NRMSE of  $R_{n.sw}$  (NRSME. $R_{n.sw}$  in Table 8 in Section 4.3) is for the soot and oceanic components. Their imaginary part of the refractive index differs significantly from the  $R_i$  of the dust-like, the basic component selected as a reference from the reflectance validation; whereas for radiative remote sensing products,  $dV(r)/dln(r)$  seems to be negligible. The lower NRSME. $R_{n.sw}$  in Table 8 for  $R_{n.sw}$  retrieved by the water-soluble component shows that a fine-mode aerosol (water-soluble) and a coarse-mode aerosol (dust-like) with similar imaginary parts of the refractive index (right plot of Figure 2) have the same radiative impact on the satellite-derived products. In the case study, a rough selection of the aerosol type can produce a maximum percent error of 14% (Table 8) in the retrieval of the  $R_{sw,n}$  for low values of  $\tau_{550}$  products (Table 2).

The radiative impact of the aerosol on the whole procedure is well described by the size distribution, and the real and imaginary parts of the refractive index become a requirement for the retrieval of land-atmosphere energy exchange, especially if the visible spectral domain is involved. Thus, the aerosol microphysical properties improve the accuracy of the spectral indices, such as

the Photosynthetically-Active Radiation (PAR) and the Leaf Area Index (LAI), driven by the energy exchange and aimed at the productivity of land and coastal ecosystems. Also worth mentioning is the increasing in the accuracy of the total net radiation,  $R_n$ , which is the key driving force for evapotranspiration coupled with the soil heat flux [56], if the longwave net radiation,  $R_{n.lw}$ , is combined with the  $R_{n.sw}$  achieved by considering the aerosol types.

We plan to complete the analysis of the radiative impact of aerosols on satellite-derived products by applying this procedure in other aerosol loading conditions taking into account the vertical distribution of the aerosol. This procedure is also the first step in involving the new generation of Earth Observation sensors for the retrieval of shortwave net radiation at a higher spatial resolution, although further research is needed to overcome the spectral homogeneity conditions.

**Acknowledgments:** The authors would like to thank the AERONET network and the principal investigators, as well as their staff, for establishing and maintaining the Cairo and El Farafra AERONET stations. The AERONET Sun photometers at El Farafra and Cairo\_EMA\_2 stations have been calibrated within the AERONET Europe TNA, supported by the European Community-Research Infrastructure Action under the FP7 ACTRIS Grant Agreement No. 262254. We are grateful to the anonymous reviewers for their valuable suggestions and helpful comments.

**Author Contributions:** Cristiana Bassani conceived of the presented work, developed the OLI@CRI algorithm, adapted the 6SV model for the purposes of this paper and worked on the atmospheric and radiative data. Ciro Manzo performed the collection of OLI and MODIS data, the coregistration of the remote sensing data, the validation of the OLI@CRI surface reflectance and the calculation of land surface albedo. Emilio Cuevas-Agulló and Ashraf Zakey contributed to providing the AERONET direct and inverse products of the Cairo\_EMA\_2 station.

**Conflicts of Interest:** The authors declare no conflict of interest.

## References

1. The Intergovernmental Panel on Climate Change (IPCC). *The Physical Science Basis. IPCC Fourth Assessment Report: Climate Change 2007 (AR4)*; IPCC: Geneva, Switzerland, 2007.
2. Haywood, J.; Boucher, O. Estimates of the direct and indirect radiative forcing due to tropospheric aerosols: A review. *Rev. Geophys.* **2000**, *38*, 513–543.
3. D’Almeida, G.A.; Koepke, P.; Shettle, E.P. *Atmospheric Aerosols: Global Climatology and Radiative Characteristics*; A. DEEPAK Publishing: Hampton, VA, USA, 1991.
4. IPCC. *The Physical Science Basis. IPCC Fifth Assessment Report: Climate Change 2013 (AR5)*; IPCC: Geneva, Switzerland, 2013.
5. Mira, M.; Olioso, A.; Gallego-Elvira, B.; Courault, D.; Garrigues, S.; Marloie, O.; Hagolle, O.; Guillevic, P.; Boulet, G. Uncertainty assessment of surface net radiation derived from Landsat images. *Remote Sens. Environ.* **2016**, *175*, 251–270.
6. Yu, H.; Kaufman, Y.J.; Chin, M.; Feingold, G.; Remer, L.A.; Anderson, T.L.; Balkanski, Y.; Bellouin, N.; Boucher, O.; Christopher, S.; et al. A review of measurement-based assessments of the aerosol direct radiative effect and forcing. *Atmos. Chem. Phys.* **2006**, *6*, 613–666.
7. Barkstrom, B.R.; Smith, G.L. The Earth Radiation Budget Experiment: Science and implementation. *Rev. Geophys.* **1986**, *24*, 379–390.
8. Harries, J.E.; Russell, J.; Hanafin, J.; Brindley, H.; Futyan, J.; Rufus, J.; Kellock, S.; Matthews, G.; Wrigley, R.; Last, A.; et al. The geostationary earth radiation budget project. *Bull. Am. Meteorol. Soc.* **2005**, *86*, doi:10.1175/BAMS-86-7-945.
9. Yu, H.; Dickinson, R.E.; Chin, M.; Kaufman, Y.J.; Zhou, M.; Zhou, L.; Tian, Y.; Dubovik, O.; Holben, B.N. Direct radiative effect of aerosols as determined from a combination of MODIS retrievals and GOCART simulations. *J. Geophys. Res. Atmos.* **2004**, *109*, doi:10.1029/2003JD003914.
10. Schaaf, C.B.; Gao, F.; Strahler, A.H.; Lucht, W.; Li, X.; Tsang, T.; Strugnell, N.C.; Zhang, X.; Jin, Y.; Muller, J.P.; et al. First operational BRDF, albedo nadir reflectance products from MODIS. *Remote Sens. Environ.* **2002**, *83*, 135–148.
11. Boucher, O.; Tarré, D. Estimation of the aerosol perturbation to the Earth’s Radiative Budget over oceans using POLDER satellite aerosol retrievals. *Geophys. Res. Lett.* **2000**, *27*, 1103–1106.
12. Drusch, M.; Bello, U.D.; Carlier, S.; Colin, O.; Fernandez, V.; Gascon, F.; Hoersch, B.; Isola, C.; Laberinti, P.; Martimort, P.; et al. Sentinel-2: ESA’s Optical High-Resolution Mission for GMES Operational Services. *Remote Sens. Environ.* **2012**, *120*, 25–36.

13. Roy, D.; Wulder, M.; Loveland, T.R.; Woodcock, C.E.; Allen, R.; Anderson, M.; Helder, D.; Irons, J.; Johnson, D.; Kennedy, R.; et al. Landsat-8: Science and product vision for terrestrial global change research. *Remote Sens. Environ.* **2014**, *145*, 154–172.
14. Masek, J.; Vermote, E.; Saleous, N.E.; Wolfe, R.; Hall, F.G.; Huemmrich, K.F.; Gao, F.; Kutler, J.; Teng-Kui, L. A Landsat surface reflectance dataset for North America, 1990–2000. *IEEE Geosci. Remote Sens. Lett.* **2006**, *3*, 68–72.
15. Franch, B.; Vermote, E.; Claverie, M. Intercomparison of Landsat albedo retrieval techniques and evaluation against in situ measurements across the US SURFRAD network. *Remote Sens. Environ.* **2014**, *152*, 627–637.
16. Deuzé, J.L.; Bréon, F.M.; Devaux, C.; Goloub, P.; Herman, M.; Lafrance, B.; Maignan, F.; Marchand, A.; Nadal, F.; Perry, G.; et al. Remote sensing of aerosols over land surfaces from POLDER-ADEOS-1 polarized measurements. *J. Geophys. Res. Atmos.* **2001**, *106*, 4913–4926.
17. Wanner, W.; Li, X.; Strahler, A.H. On the derivation of kernels for kernel-driven models of bidirectional reflectance. *J. Geophys. Res. Atmos.* **1995**, *100*, 21077–21089.
18. Mielonen, T.; Levy, R.C.; Aaltonen, V.; Komppula, M.; de Leeuw, G.; Huttunen, J.; Lihavainen, H.; Kolmonen, P.; Lehtinen, K.E.J.; Arola, A. Evaluating the assumptions of surface reflectance and aerosol type selection within the MODIS aerosol retrieval over land: the problem of dust type selection. *Atmos. Meas. Tech.* **2011**, *4*, 201–214.
19. Roman, M.O.; Gatebe, C.K.; Shuai, Y.; Wang, Z.; Gao, F.; Masek, J.G.; He, T.; Liang, S.; Schaaf, C.B. Use of in Situ and Airborne Multiangle Data to Assess MODIS- and Landsat-Based Estimates of Directional Reflectance and Albedo. *IEEE Trans. Geosci. Remote Sens.* **2013**, *51*, 1393–1404.
20. Kaufman, Y.J.; Tanré, D.; Remer, L.A.; Vermote, E.F.; Chu, A.; Holben, B.N. Operational remote sensing of tropospheric aerosol over land from EOS moderate resolution imaging spectroradiometer. *J. Geophys. Res.* **1997**, *102*, 17051–17067.
21. Vermote, E.F.; Saleous, N.E.; Justice, C.; Kaufman, Y.; Privette, J.; Remer, L.; Roger, J.; Tanré, D. Atmospheric correction of visible to middle-infrared EOS-MODIS data over land surfaces: Background, operational algorithm and validation. *J. Geophys. Res.* **1997**, *102*, 675–686.
22. Justice, C.; Townshend, J.; Vermote, E.; Masuoka, E.; Wolfe, R.; Saleous, N.; Roy, D.; Morisette, J. An overview of MODIS Land data processing and product status. *Remote Sens. Environ.* **2002**, *83*, 3–5.
23. Myneni, R.; Hoffman, S.; Knyazikhin, Y.; Privette, J.; Glassy, J.; Tian, Y.; Wang, Y.; Song, X.; Zhang, Y.; Smith, G.; et al. Global products of vegetation leaf area and fraction absorbed PAR from year one of MODIS data. *Remote Sens. Environ.* **2002**, *83*, 214–231.
24. Kotchenova, S.Y.; Vermote, E.F.; Levy, R.; Lyapustin, A. Radiative transfer codes for atmospheric correction and aerosol retrieval: Intercomparison study. *Appl. Opt.* **2008**, *47*, 2215–2226.
25. Vermote, E.F.; Tanré, D.; Deuzé, J.L.; Herman, M.; Morcrette, J.J.; Kotchenova, S.Y. Second Simulation of a Satellite Signal in the Solar Spectrum-Vector (6SV). Available online: <http://6s.ltdri.org> (accessed on 23 August 2016).
26. Vermote, E.F.; Tanré, D.; Deuzé, J.L.; Herman, M.; Morcrette, J.J. Second simulation of the satellite signal in the solar spectrum, 6S: An overview. *IEEE Trans. Geosci. Remote Sens.* **1997**, *35*, 675–686.
27. Berk, A.; Bernstein, L.; Anderson, G.; Acharya, P.; Robertson, D.; Chetwynd, J.; Adler-Golden, S. MODTRAN Cloud and Multiple Scattering Upgrades with Application to AVIRIS. *Remote Sens. Environ.* **1998**, *65*, 367–375.
28. Kokhanovsky, A.A. *Aerosol Optics: Light Absorption and Scattering by Particles in the Atmosphere*; Praxis Publishing Ltd.: Chichester, UK, 2008.
29. Holben, B.; Eck, T.; Slutsker, I.; Tanré, D.; Buis, J.; Setzer, A.; Vermote, E.; Reagan, J.; Kaufman, Y.; Nakajima, T.; et al. AERONET—A Federated Instrument Network and Data Archive for Aerosol Characterization. *Remote Sens. Environ.* **1998**, *66*, 1–16.
30. Dubovik, O.; Smirnov, A.; Holben, B.N.; King, M.D.; Kaufman, Y.J.; Eck, T.F.; Slutsker, I. Accuracy assessments of aerosol optical properties retrieved from Aerosol Robotic Network (AERONET) Sun and sky radiance measurements. *J. Geophys. Res. Atmos.* **2000**, *105*, 9791–9806.
31. King, M.D.; Kaufman, Y.J.; Tanré, D.; Nakajima, T. Remote sensing of tropospheric aerosols from space: Past, present, and future. *Bull. Am. Meteorol. Soc.* **1999**, *88*, 2229–2259.
32. Dubovik, O.; Holben, B.; Eck, T.F.; Smirnov, A.; Kaufman, Y.J.; King, M.D.; Tanré, D.; Slutsker, I. Variability of Absorption and Optical Properties of Key Aerosol Types Observed in Worldwide Locations. *J. Atmos. Sci.* **2002**, *59*, 590–608.

33. Tanré, D.; Kaufman, Y.J.; Herman, M.; Mattoo, S. Remote sensing of aerosol properties over oceans using the MODIS/EOS spectral radiances. *J. Geophys. Res. Atmos.* **1997**, *102*, 16971–16988.
34. Kokhanovsky, A.A.; Deuzé, J.L.; Diner, D.J.; Dubovik, O.; Ducos, F.; Emde, C.; Garay, M.J.; Grainger, R.G.; Heckel, A.; Herman, M.; et al. The inter-comparison of major satellite aerosol retrieval algorithms using simulated intensity and polarization characteristics of reflected light. *Atmos. Meas. Tech.* **2010**, *3*, 909–932.
35. Kaufman, Y.J.; Wald, A.; Remer, L.A.; Gao, B.C.; Li, R.R.; Flynn, L. The MODIS 2.1  $\mu\text{m}$  channel—correlation with visible reflectance for use in remote sensing of aerosol. *IEEE Trans. Geosci. Remote Sens.* **1997**, *35*, 1286–1298.
36. Kaufman, Y.J.; Tanré, D.; Gordon, H.R.; Nakajima, T.; Lenoble, J.; Frouin, R.; Grassl, H.; Herman, B.M.; King, M.; Teillet, P.M. Passive remote sensing of tropospheric aerosol and atmospheric correction for the aerosol effect. *J. Geophys. Res.* **1997**, *102*, 16815–16830.
37. Remer, L.A.; Tanré, D.; Kaufman, Y.J.; Ichoku, C.; Mattoo, S.; Levy, R.; Chu, D.A.; Holben, B.; Dubovik, O.; Smirnov, A.; et al. Validation of MODIS aerosol retrieval over ocean. *Geophys. Res. Lett.* **2002**, *29*, MOD3-1–MOD3-4.
38. Tirelli, C.; Curci, G.; Manzo, C.; Tuccella, P.; Bassani, C. Effect of the Aerosol Model Assumption on the Atmospheric Correction over Land: Case Studies with CHRIS/PROBA Hyperspectral Images over Benelux. *Remote Sens.* **2015**, *7*, 8391–8415.
39. Bassani, C.; Manzo, C.; Braga, F.; Bresciani, M.; Giardino, C.; Alberotanza, L. The impact of the microphysical properties of aerosol on the atmospheric correction of hyperspectral data in coastal waters. *Atmos. Meas. Tech.* **2015**, *8*, 1593–1604.
40. Levy, R.C.; Remer, L.A.; Dubovik, O. Global aerosol optical properties and application to Moderate Resolution Imaging Spectroradiometer aerosol retrieval over land. *J. Geophys. Res.* **2007**, *112*, doi:10.1029/2006JD007815.
41. Ahmad, Z.; Franz, B.A.; McClain, C.R.; Kwiatkowska, E.J.; Werdell, J.; Shettle, E.P.; Holben, B.N. New aerosol models for the retrieval of aerosol optical thickness and normalized water-leaving radiances from the SeaWiFS and MODIS sensors over coastal regions and open oceans. *Appl. Opt.* **2010**, *49*, 5545–5560.
42. IOCCG. Atmospheric Correction for Remotely-Sensed Ocean-Colour Products. In *Reports and Monographs of the International Ocean-Colour Coordinating Group*; Wang, M., Ed.; IOCCG: Dartmouth, NS, Canada, 2010; Volume 10.
43. Illingworth, A.J.; Barker, H.W.; Beljaars, A.; Ceccaldi, M.; Chepfer, H.; Clerbaux, N.; Cole, J.; Delanoë, J.; Domenech, C.; Donovan, D.P.; et al. The EarthCARE Satellite: The Next Step Forward in Global Measurements of Clouds, Aerosols, Precipitation, and Radiation. *Bull. Am. Meteorol. Soc.* **2015**, *96*, 1311–1332.
44. Pappalardo, G.; Amodeo, A.; Apituley, A.; Comeron, A.; Freudenthaler, V.; Linné, H.; Ansmann, A.; Bösenberg, J.; D’Amico, G.; Mattis, I.; et al. EARLINET: Towards an advanced sustainable European aerosol lidar network. *Atmos. Meas. Tech.* **2014**, *7*, 2389–2409.
45. Wiegner, M.; Madonna, F.; Binietoglou, I.; Forkel, R.; Gasteiger, J.; Geiß, A.; Pappalardo, G.; Schäfer, K.; Thomas, W. What is the benefit of ceilometers for aerosol remote sensing? An answer from EARLINET. *Atmos. Meas. Tech.* **2014**, *7*, 1979–1997.
46. Vaughan, M.A.; Powell, K.A.; Winker, D.M.; Hostetler, C.A.; Kuehn, R.E.; Hunt, W.H.; Getzewich, B.J.; Young, S.A.; Liu, Z.; McGill, M.J. Fully Automated Detection of Cloud and Aerosol Layers in the CALIPSO Lidar Measurements. *J. Atmos. Ocean. Technol.* **2009**, *26*, 2034–2050.
47. Winker, D.M.; Vaughan, M.A.; Omar, A.; Hu, Y.; Powell, K.A.; Liu, Z.; Hunt, W.H.; Young, S.A. Overview of the CALIPSO Mission and CALIOP Data Processing Algorithms. *J. Atmos. Ocean. Technol.* **2009**, *26*, 2310–2323.
48. Bassani, C.; Cavalli, R.M.; Pignatti, S. Aerosol optical retrieval and surface reflectance from airborne remote sensing data over land. *Sensors* **2010**, *10*, 6421–6438.
49. Kokhanovsky, A.A.; De Leeuw, G. *Satellite Aerosol Remote Sensing Over Land*; Springer: Berlin, Germany; Heidelberg, Germany, 2009.
50. Shuai, Y.; Masek, J.G.; Gao, F.; Schaaf, C.B. An algorithm for the retrieval of 30-m snow-free albedo from Landsat surface reflectance and MODIS BRDF. *Remote Sens. Environ.* **2011**, *115*, 2204–2216.
51. Feng, M.; Huang, C.; Channan, S.; Vermote, E.F.; Masek, J.G.; Townshend, J.R. Quality assessment of Landsat surface reflectance products using MODIS data. *Comput. Geosci.* **2012**, *38*, 9–22.
52. Vermote, E.F.; Kotchenova, S. Atmospheric correction for the monitoring of land surfaces. *J. Geophys. Res. Atmos.* **2008**, *113*, doi:10.1029/2007jd009662.

53. Arabas, S.; Schellens, M.; Coulais, A.; Gales, J.; Messmer, P. GNU Data Language (GDL)—A free and open-source implementation of IDL. In Proceedings of the EGU General Assembly 2010, Vienna, Austria, 2–7 May 2010; p. 924.
54. Barsi, J.A.; Lee, K.; Kvaran, G.; Markham, B.L.; Pedelty, J.A. The Spectral Response of the Landsat-8 Operational Land Imager. *Remote Sens.* **2014**, *6*, 10232–10251.
55. Bassani, C.; Cavalli, R.M.; Antonelli, P. Influence of aerosol and surface reflectance variability on hyperspectral observed radiance. *Atmos. Meas. Tech.* **2012**, *5*, 1139–1203.
56. Bisht, G.; Venturini, V.; Islam, S.; Jiang, L. Estimation of the net radiation using MODIS (Moderate Resolution Imaging Spectroradiometer) data for clear sky days. *Remote Sens. Environ.* **2005**, *97*, 52–67.



© 2016 by the authors; licensee MDPI, Basel, Switzerland. This article is an open access article distributed under the terms and conditions of the Creative Commons Attribution (CC-BY) license (<http://creativecommons.org/licenses/by/4.0/>).